Manuscript File Click here to view linked References

On the deflection of the liquid−vapor interface in a wicked heat pipe

Muhammad Rizwanur Rahman*, Prashant R. Waghmare and M. R. Flynn

Department of Mechanical Engineering, University of Alberta, Edmonton T6G 1H9, Canada

*Corresponding author: mrahman6@ualberta.ca

Abstract

The shape of the liquid-vapor interface along the length of the adiabatic section of a heat pipe - a passive heat transfer device that relies on capillary pumping - is investigated to identify the mechanisms behind both performance enhancement techniques as well as operational failure. In formulating the associated mathematical model, the liquid flow within the (screen type) wick is described using Darcy's law while Poiseuille's equation is applied for the vapor phase. The liquid and vapor phases are coupled together using the Young-Laplace equation with additional closure provided by select thermodynamic relations e.g. to relate the temperature and pressure changes experienced by the vapor. Our model thereby predicts the shape of the liquid-vapor interface and its deflection owing to the variations in the heat load, operating temperature and the wick-surface characteristics. Together, these details can prescribe the parameter space over which the liquid-vapor interface remains mechanically-stable meaning that the heat pipe can function effectively. The possibility of employing a wick with non-uniform wetting characteristics is also explored with comparisons drawn against the uniform wettability case. The comparison in question reveals some of the benefits of the former approach. For instance, a wick exhibiting a contact angle that varies as a function of the axial coordinate allows for better control of (i) the depth to which the interface is recessed within the wires comprising the wick, and, therefore (ii) the entrainment of liquid droplets into the counter-flowing vapor stream. As such, the space of acceptable operating parameters can be suitably expanded.

Keywords: Heat pipe, wettability gradient, wick, interface, capillary pressure, entrainment, recess depth.

1 Introduction

Owing to the central importance of wetting phenomena in a broad spectrum of natural and technological processes, the past two decades have seen a large increase of interest in wettability and the formation, deformation and translation of droplets and bubbles across solid surfaces (Mingjie et al. 2010, Lafuma & Quéré 2003, Gao et al. 2009). Surfaces may be characterized in terms of their affinity for various fluids e.g. oil, air and water. In the latter case, the two extremes of wettability are (super-) hydrophilic and (super-) hydrophobic surfaces - both are abundant in nature from the cornea of human eye (Lemp et al. 1970) to Lotus leaves (Fürstner et al. 2005, Quéré & Reyssat 2008) to the textured waxy surfaces of water-walking arthropods (Bush et al. 2008) to insect wings (Polet et al. 2015). Discoveries of such functional surfaces in nature have led to advances in microfluidic devices (Abate et al. 2010) and to the fabrication of surfaces with various functionalities, primarily driven by liquid - repellent characteristics, e.g., anti-fouling, anti-fogging (Drelich et al. 2011), drag reduction (McHale et al. 2011, Rastegari & Akhavan 2015, Hu et al. 2017) and self-cleaning (Blossey 2003), to name a few.

In recent years, multi-functional surfaces that are rendered, in pattern formation, both hydrophobic and hydrophilic, have shown great potential in fabricating pump-free micro-fluidic devices (Kobayashi et al. 2011) or systems capable of highly-accurate liquid metering (Lee et al. 2002), controlled liquid spreading (Feng et al. 2014) or enhanced heat transfer by condensation (Daniel et al. 2001). This latter example is of particular interest here because of the central importance of condensation (and evaporation) to heat pipes, passive devices designed to transfer heat, often in large quantities, between a thermal source and sink. In its simplest incarnation, a heat pipe is a thermal conductance device consisting of a hollowed-out metal cylinder inside of which is a liquid in equilibrium with its vapor. One end of the cylinder is affixed to a hot surface or placed in a stream of hot fluid causing the interior liquid to evaporate. The vapor then travels the length of the cylinder to the opposite end where condensation occurs. Given the large amounts of heat absorbed or released by phase change, heat pipes can achieve rates of heat transfer that are orders of magnitude larger than those due to simple conduction (Reay et al. 2013). As a result, heat pipes are now deployed in a multitude of configurations and in numerous applications from building heat recovery to the passive cooling of electronic and aerospace components (Vafai & Wang 1992, Shafahi et al. 2010, Faghri 2012).

Key to the successful operation of a heat pipe is capillary pumping, which depends on the curvature of the liquid-vapor interface and is responsible for ensuring that an adequate volume of liquid is returned to the evaporator. Indeed, and as regards heat pipe performance, the capillary pumping limit is typically considered as the gravest of the five limiting factors, the others being the sonic limit, the boiling limit, the entrainment limit and the viscous limit (Faghri 2012, Reay et al. 2013). As the source-to-sink temperature difference increases and the capillary limit is approached, there develops an uneven distribution of the liquid along interior surfaces (Mwaba et al. 2006). Such non-uniformities lead to "dry out", which is associated with a significant and sudden drop in the axial heat flux (Chi 1976).

Given the importance of capillary pumping and the interfacial pressure difference (to

say nothing of the voluminous scientific literature on heat pipe design and operation), it is surprising that more attention has not been devoted to understanding the geometric details of the interface, pressure difference and interface deflection being related one to the other through the Young-Laplace equation. Here, we seek to address this knowledge gap by studying, theoretically, the liquid-vapor interface along the adiabatic section of a heat pipe. Attention is focused on heat pipes having a screen type wick, these being simpler and more cost effective than many other wicks when considering terrestrial and comparatively low-temperature applications (Reay et al. 2013). In this formulation, we relax the popular simplification that the three phase contact point is somehow anchored at a fixed elevation within the wick e.g. along the equatorial plane of the wires comprising the wick. We further examine the underlying physics that dictate the manner in which the interface deflects owing to variations of the thermodynamic conditions and wetting characteristics of the wick.

Understanding the aforementioned geometric details is a topic of both fundamental and practical interest. For instance, the model developed in this study prescribes the parametric regimes where a mechanically-stable liquid-vapor interface can and cannot form. Wu & Peterson (1991) and Khrustalev & Faghri (1994) showed that enhancing capillarity by making the wick more hydrophilic can increase heat pipe performance. On the other hand, heat pipes so treated may suffer from a lower rate of condensation, which must then occur in a film-wise rather than a drop-wise fashion (Rykaczewski et al. 2014). Such constraints can be avoided by the application of a heterogeneous surface chemical treatment and, to this end, our model can be used to quantitatively characterize some of the associated benefits. The present work is therefore complementary to the laboratory investigations of Hu et al. (2013) and numerical study of Singh et al. (2017, 2018) who found improved thermal performance for heat pipes containing chemically-heterogeneous wicks.

The rest of the manuscript is organized as follows: in section 2, we develop a model to relate the interfacial geometry to the thermo-fluid dynamics with select technical details explained in appendices A, B and C. In section 3, we apply the so-derived model to explore how variations of temperature, wick geometry and, perhaps most importantly, wettability effect the shape of the liquid-vapor interface that forms between adjacent wires from within the wick. The (nontrivial) extrapolation of our results from the space between adjacent wires to the entire length of the heat pipe adiabatic section is explored in section 4. Finally, in section 5, we present conclusions and ideas for future research.

2 Modelling the liquid-vapor interface shape

The present study pays particular attention to the deflection of the liquid-vapor interface between the evaporator and condenser ends of the adiabatic section. To predict this deflection analytically and thereby estimate the interface shape, geometric details are considered in conjunction with the relevant thermo-fluid dynamics.

2.1 Thermo−fluid analysis

Interface curvature derives from the capillary pressure, P_c, due to the imbalance of pressure between the vapor and liquid phases. More precisely, P_c can be related to the interface curvature using the Young-Laplace equation, the general one-dimensional form of which is given by

$$\frac{P_c}{\sigma} = -\nabla.\mathbf{n} = \frac{\eta_{xx}}{\left(1+\eta_x^2\right)^{3/2}} \tag{1}$$

where σ is the surface tension, $\mathbf{n}$ the unit normal vector, $\eta(x)$ is a function that defines the interface shape and subscripts indicate derivatives. Obvious from the above equation, and throughout the study, steady state operation is assumed. The liquid and vapor pressure, and therefore also $P_c = P^v - P^l$, change with x due to friction. To this end, the vapor pressure drop between the two ends of the adiabatic section can be approximated by the Hagen–Poiseuille equation as

$$\Delta P^v = \frac{8\dot{m}\mu_v L_a}{\pi\rho_v R_v^4} \tag{2}$$

where L_a and R_v denote, respectively, the length of the (cylindrical) adiabatic section and the vapor core radius. Moreover, $\dot{m} = Q/h_{\mathrm{fg}}$ is the mass flux in which Q is the heat flux and h_{fg} is the latent heat of vaporization. The fluid properties, *i.e.*, viscosity (μ_v), density (ρ_v) and h_{fg} are evaluated at the heat pipe operating temperature, T_{op}, which is obtained from the thermal resistance network model outlined in Appendix B.

For pragmatic purposes, it is oftentimes preferable to replace the pressure drop of (2) with a temperature drop, ΔT^v, pressure and temperature changes following one from the other. For this purpose, the Clausius-Clapeyron equation is often applied (Brown 1951). Although the Clausius-Clayperon equation is generally regarded as accurate for small ΔT^v, it does not consider the temperature dependence of h_{fg} and so is not as precise as the semi-empirical Magnus equation, which reads (Alduchov & Eskridge 1996, Jenkins 2008)

$$P^v = C_1 \exp\left[\frac{C_2 T^v}{C_3 + T^v}\right] \tag{3}$$

In (3), the C_i's are empirical constants that vary depending on the chemical composition of the working fluid. For instance, if the working fluid is water, then $C_1 = 6.1094 \times 10^2$ Pa, $C_2 = 17.625$ and $C_3 = 243.04$°C, when pressure and temperature are expressed, respectively, in Pa and °C (Alduchov & Eskridge 1996). With these values to hand, and by differentiating (3), it is straightforward to relate ΔP^v to ΔT^v. Thus if the axial heat flux and operating temperature are known (e.g. from the aforementioned thermal resistance network model), the pressure and temperature drop along the core of the heat pipe can be respectively estimated from (2) and (3).

On the wick side of the heat pipe, as liquid returns from the condenser to the evaporator due to capillary pumping, the axial pressure drop, ΔP^l, can be approximated by Darcy's law (Reay et al. 2013), *i.e.,*

$$\Delta P^l = \frac{\mu_l L_a \dot{m}}{\rho_l A_w K} \tag{4}$$

Here, μ_l and ρ_l are, respectively, the viscosity and density of the liquid measured at T_{op}. Meanwhile, A_w and K denote, respectively, the wick cross sectional area and permeability. For the case of the screen-type wick illustrated in figure 1 below, K can be evaluated from (Peterson 1994)

$$K = \frac{D^2\,\epsilon^3}{122\,(1-\epsilon)^2} \tag{5}$$

where ϵ is wick porosity and D is wire diameter.

The adiabatic section, which plays a significant role in the stable operation of a heat pipe (Brahim & Jemni 2014), is the primary focus of this study. In modelling the interfacial deflection along the adiabatic section of the heat pipe, we select a co-ordiante system such that $x = 0$ denotes the starting point of the adiabatic section at the end of the evaporator. Meanwhile $x = l$ indicates ending point of the adiabatic section at the beginning of the condenser. Henceforth, we will refer to these points as the 'evaporator end' ($x = 0$) and the 'condenser end' ($x = l$), respectively. The flow of liquid and vapor being anti-parallel, the vapor and liquid pressures respectively reach their maximum and minimum values at the evaporator end. The resulting pressure difference causes the liquid-vapor interface to deform in a convex fashion – see e.g. figure 1. An interfacial deflection is also possible at the condenser end, $x = l$. Provided, however, that the temperature variation is fairly modest in the adiabatic section, which is reasonable when considering low temperature applications such as building heat recovery and electronic cooling, the liquid and vapor often exhibit nearly equal pressures, i.e. $P^l(l) \simeq P^v(l)$. Consequently, the liquid−vapor interface can be assumed flat at the condenser end (Faghri 2012). For $0 \leq x \leq l$, pressure drops on the liquid and vapor side of the interface can now be summed to obtain the capillary pressure at a given axial location. More specifically

$$P_c(0) = P^v(0) - P^l(0) = \Delta P^v + \Delta P^l \tag{6}$$

$$P_c(x) \equiv P^v(x) - P^l(x) = \Big(\Delta P^v + \Delta P^l\Big)\left(1 - \frac{x}{l}\right) = P_c(0)\Big(1 - \frac{x}{l}\Big) \tag{7}$$

Implicit in the above equations is the notion that the heat pipe inner diameter, d_i, (or equivalently the Bond number, $\text{Bo} = (\rho_l - \rho_v)gd_i/(\sigma/R)$ where g is gravitational acceleration and R is the radius of curvature defined in figure 1) is sufficiently small so that, for any x, the liquid pressure is approximately the same along the upper and lower surfaces of the heat pipe. Of course, we further assume, consistent with figure 1, a horizontal heat pipe. When the heat pipe is instead inclined, a hydrostatic correction term must be applied in (7). We omit such (straightforward) details for brevity.

The capillary pressure dictates the shape of the liquid-vapor interface and acts as the key driving force for the liquid flow. Therefore, upon the capillary pressure must depend a number of essential performance parameters, *e.g.,* the maximum heat flux and the dry-out limit. Describing the interface deflection is therefore crucial in assessing the impact of different geometric and thermodynamic parameters on the effective functioning of a heat pipe. These ideas are expanded upon in the following sub-sections.

2.2 Geometric modelling of the liquid−vapor interface

We consider a screen-type wick, saturated with working fluid, which consists of cylindrical wires placed circumferentially along the length of the heat pipe (see figure 1). Consistent with the latter equality in (1) and with previous studies on this (Singh et al. 2017) and related (Flynn & Bush 2008) topics, the influence of the wires aligned parallel to the axis of the heat pipe is ignored for simplicity. The influence of such wires could be accounted for by generalizing (1) to its two-dimensional analogous form such that the radii of curvature in both the transverse and the axial directions are included. Such a step would increase the magnitude of the capillary pressure but would not otherwise change the essential details of our analyses.

A schematic is presented in figure 1 that shows, in the inset, the details of the interface that forms between two adjacent wires. Borrowing notation from Flynn & Bush (2008), the wire diameter represented as D and the center-to-center spacing between adjacent wires is β (note that β is the inverse of the mesh number, $\mathcal{N}$, where $\mathcal{N}$ designates the number of wires per unit length of the wick). From this point forward, we will refer to the liquid-vapor interface formed within a single cell consisting of two adjacent wires as the meniscus. The summation of all of the menisci constitutes the liquid-vapor interface. The meniscus forms an equilibrium contact angle of θ with the tangent drawn at the triple point. Meanwhile, the angle the meniscus makes with a horizontal line drawn at the triple point is denoted by ϕ; we shall hereafter refer to ϕ as the interface angle. Note finally that the offset distance of the top-most wires from the inner wall of the heat pipe is d_{off}. Throughout this study, d_{off} is set to 15 times the wire diameter.

Typically, wicks consist of wires that are thin and tightly spaced. Hence, in modelling the meniscus, it is justified to assume a spherical cap or, for the particular geometry considered here, a circular cap (Reay et al. 2013). As such, (1) can be simplified to read:

$$\frac{P_c}{\sigma} = \frac{1}{R} \tag{8}$$

Implicit in (8) are three key assumptions. For low temperature applications featuring a modest source-to-sink temperature difference, an operating temperature ranging from 122 K-628 K (Chi 1976) and excluding cryogenic or liquid-metal heat pipes, the vapor velocity is comparatively low, which results in Weber numbers, We, less than unity. Symbolically, we write

$$\text{We} = \frac{\rho_v v_v^2 \beta}{\sigma} < 1\,,$$

here v_v is the vapor velocity. In such a parametric regime, inertial effects are dominated by surface tension effects and the interface remains relatively stable (Ishii & Grolmes 1975). Stated differently, the effect of the bulk flow on the interface is small. We further assume that the facing semi-circles of adjacent wire pairs have the same wettability as characterized by an (equal) contact angle, θ. In other words, and with reference to figure 1, the eastern semi-circle of a particular wire has the same contact angle as the western semi-circle of the wire lying just to its right. Finally, we assume a pure working fluid and a smooth, homogeneous and rigid wire surface such that θ always assumes its (unique) equilibrium value.

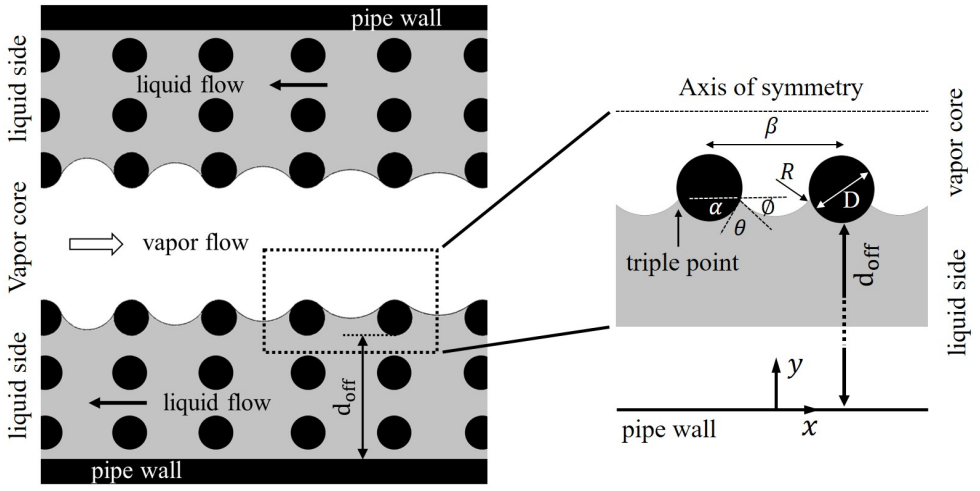


Figure 1: Schematic of a segment of a heat pipe adiabatic section (not to scale) showing the porous wick and the central core. The zoomed view shows the details of the meniscus formed between two adjacent wires. Only the upper most wire layer is shown in the inset image because the lower layers of the porous wick do not directly affect the interface.

Considering the assumptions outlined in the previous paragraph, and following some straightforward geometric steps (see Appendix A and Flynn & Bush 2008), the following relationship between the interface curvature, R, the wick geometry and the contact angle can be derived:

$$R = \frac{\beta}{2\sin\phi}\left[1 - \frac{D}{\beta}\sin\left(\theta + \phi\right)\right] \tag{9}$$

Solving for ϕ, we find the following three solutions to (9):

$$\phi_1 = 2\arctan\left[\frac{-\sqrt{4R^2 + 4RD\cos\theta + D^2 - \beta^2} + 2R + D\cos\theta}{D\sin\theta + \beta}\right] \tag{10a}$$

$$\phi_2 = 2\arctan\left[\frac{+\sqrt{4R^2 + 4RD\cos\theta + D^2 - \beta^2} + 2R + D\cos\theta}{D\sin\theta + \beta}\right] \tag{10b}$$

$$\phi_3 = 2\arctan\left[\frac{\beta}{2R + D\cos\theta}\right] \tag{10c}$$

Note, however, that the solutions associated with ϕ_2 and ϕ_3 are unphysical. In the former case, the meniscus curvature is concave rather than convex. In the latter case, the meniscus is mechanically-unstable in the sense of Princen (1969) – see Appendix C. Equation (10 a) prescribes the lone physical solution, but in order that it admit realistic results, the following solvability criterion must be satisfied:

$$4R^2 + 4RD\cos\theta + D^2 \geq \beta^2 \tag{11}$$

For the special case where $\theta = 0°$, the above criterion reduces to $2R \geq \beta - D$. That is, the minimum radius of curvature, $R_{\min} = (\beta - D)/2$, is such that the meniscus just touches the equatorial planes of the adjacent wires. If the pressure drop across the meniscus is too large such that, by (8), $R < R_{\min}$, the meniscus no longer satisfies (11) and hence, no solution to (10 a) is possible. Conversely, and for large R (and large ϕ), a meniscus should be barred from overlapping with its neighbouring menisci, this to avoid a detachment of the liquid from the solid phase.

3 Results – local analysis

Once the capillary pressure distribution is known from the thermo-fluid analysis, the geometric model of section 2.2, in conjunction with (8), can be combined to determine the variation of the interface shape as a function of the axial coordinate, x. Coupling the thermo-fluid and geometric models in this way provides a novel opportunity to critically assess the significance of a number of key parameters vis-à-vis heat pipe performance.

3.1 Role of temperature

The influence of temperature on the functioning of a heat pipe can be scrutinized in two different ways: (i) by varying the operating temperature (T_{op}) without adjusting the source-to-sink temperature difference (ΔT), and, (ii) by varying ΔT but not T_{op}. We consider each of these possibilities in turn. For fixed ΔT, increasing the operating temperature causes a decrease in the thermal resistance, R_{eq} (Appendix B), which thereby increases the heat flux, Q ($= \Delta T/R_{\text{eq}}$). The increment in T_{op} is accompanied also by variations in the fluid properties. For instance, μ_l, ρ_l and h_{fg} decrease with increasing T_{op} resulting, overall, in a decrease in ΔP^l – see (4). In the vapor phase, meanwhile, μ_v increases with T_{op} but so too does ρ_v resulting, overall, in a decrease of ΔP^v – see (2). Consequently, and as predicted by (6) and (7), P_c decreases when T_{op} increases. As a result of this decrease of capillary pressure, (8) requires that the meniscus radius of curvature increase and this, in turn, causes variations in the meniscus length, λ, and recess depth, δ_R, which are defined schematically in figure 2.

When the source-to-sink temperature difference, ΔT, increases for the same T_{op}, Q must again increase. Fluid velocities must likewise increase along with the associated pressure drops, resulting in a larger capillary pressure. Although this line of reasoning is not pursued here, information about pressure (and temperature) changes can also be inferred by an examination of the temperature-entropy diagram. For further description of these and other thermodynamic aspects, see Richter & Gottschlich (1994) and Zuo & Faghri (1998).

As it turns out, and because of the circular geometry exhibited in figure 2, the variation of λ with T_{op} and ΔT is not entirely straightforward. Consider, for instance, figure 3 (a) which indicates that λ is a non-monotone function of T_{op} for $\Delta T = 20°\text{C}$ and 15°C but a monotone function of T_{op} for $\Delta T = 10°\text{C}$. In figure 3 (b), the $\Delta T = 20°\text{C}$ case from figure 3 (a) has been reproduced with three representative meniscus shapes (corresponding to $T_{\text{op}} = 35°\text{C}$, 45°C and 55°C) plotted in the inset. The meniscus corresponding to $T_{\text{op}} = 45°\text{C}$ is shorter than its

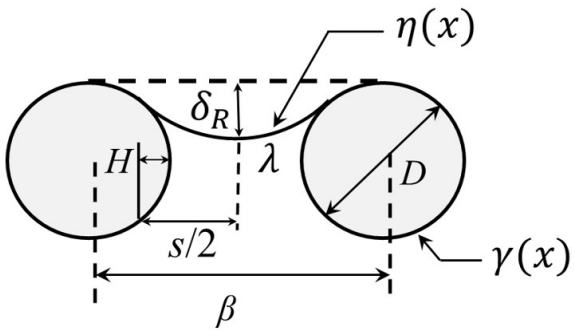


Figure 2: The meniscus length (λ) is defined as the arc length of the liquid-vapor interface between two adjacent wires. The total interface length is the sum of all such constituent lengths measured between individual wire pairs. Meanwhile, the recess depth (δ_R) is the maximum vertical distance between the meniscus, described by the function $\eta = \eta(x)$, and a horizontal line connecting the apex of the adjacent wires. Note, finally, that the wire surface is defined by the function $\gamma = \gamma(x)$.

35°C or 55°C counterparts. Indeed, because increasing the operating temperature results in a decrease in the capillary pressure, the triple point steadily moves (north) poleward as T_{op} increases from 35°C to 55°C – see figure 3 (c). The competing influences of a decrease in the radius of curvature coupled with an increase in s, the triple point separation distance causes, in figure 3 (b), the arc length to first decrease then increase with T_{op}. Correspondingly, and for this particular combination of $\theta\,(= 45^\circ)$ and $\Delta T\,(= 20^\circ\text{C})$, we realize a (global) minimum arc length of approximately 0.844β.

3.2 Role of wettability

Surface wettability adds another layer of complexity: figure 4 (a) shows the manner in which the meniscus length varies with T_{op} for fixed ΔT but different θ. When the wick is respectively hydrophilic and hydrophobic, λ increases and decreases with the operating temperature. Figures 4 (b,c) show menisci at $T_{\text{op}} = 35^\circ\text{C}, 45^\circ\text{C}$ and 55°C corresponding to contact angles of 0° and 150°, respectively. For the conditions of interest here, the meniscus for the hydrophilic wick ($\theta = 0^\circ$) locates above the equatorial plane. As the operating temperature increases, the capillary pressure decreases resulting in a flatter meniscus with a larger length. Conversely, and for $\theta = 150^\circ$, the meniscus appears strictly below the equatorial plane. A reduction of the capillary pressure is again associated with a flattening of the interface, but this now leads to a decrease, not an increase, in λ. Of course, the profiles exhibited in figure 4 (a) consider the special case of a monotone variation of λ with T_{op}. For ΔT different from 15°C (not shown), non-monotone behavior of the type exhibited in figure 3 is possible.

The role of surface wettability can be more readily appreciated from the surface plots of figure 5 (a-d) where the variation of the meniscus length is plotted against T_{op} and ΔT for four different contact angles. For instance, if we consider $\theta = 0^\circ$, the meniscus length

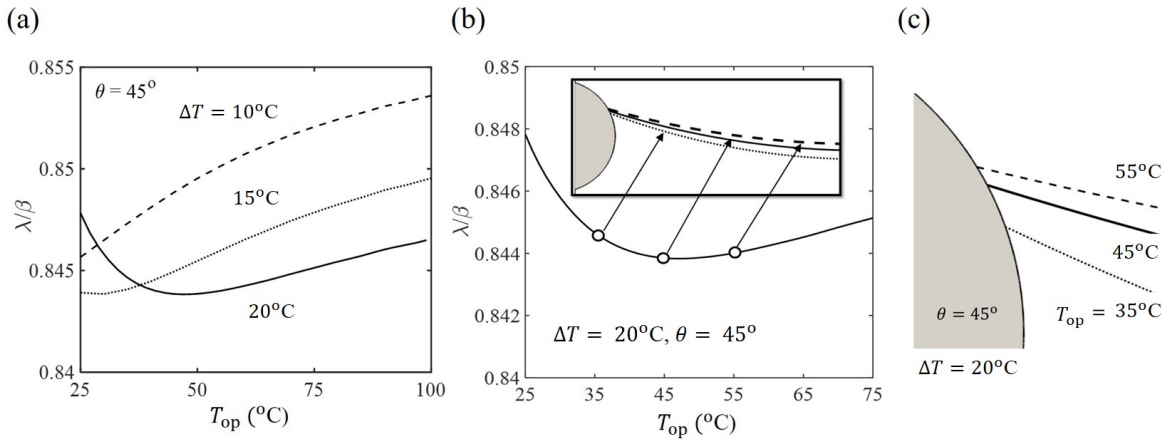


Figure 3: (a) Variation with $T_{\rm op}$ of the meniscus length (non-dimensionalized by the wire spacing β), for $\Delta T = 10$°C, 15°C and 20°C. (b) Illustration of the meniscus shape for $\Delta T = 20$°C and three different values of $T_{\rm op}$. (c) Zoomed view of the triple point locations for the wire surface illustrated in (b). Throughout, we assume $\theta = 45^\circ$ and $D/\beta = 0.35$.

decreases with increasing ΔT for larger operating temperatures but exhibits non-monotonic behavior for smaller $T_{\rm op}$. By contrast, if the wick material is rendered hydrophobic so that $\theta = 150^\circ$, the meniscus length is then an increasing function of ΔT irrespective of the operating temperature. Whereas large $T_{\rm op}$ and, more especially, small ΔT thereby guarantees the longest possible meniscus length when $\theta = 0^\circ$, this same temperature combination yields the shortest possible length when $\theta = 150^\circ$.

The evolution of the meniscus geometry as the triple point is moved along the solid surface in response to variations of ΔT, $T_{\rm op}$ or θ can be further understood with reference to δ_R, which is defined schematically in figure 2. In contrast to the meniscus length, figure 5 (e-h) shows that the recess depth exhibits a monotone variation with ΔT and $T_{\rm op}$: for fixed ΔT, the capillary pressure increases with decreasing $T_{\rm op}$, hence the meniscus adjusts downward and the recess depth increases. This behavior is pronounced for large ΔT but comparatively insignificant as the source temperature approaches the sink temperature. Conversely, and for fixed $T_{\rm op}$, we find that δ_R increases with ΔT.

Figure 5 is important for another reason, i.e. it confirms that the parameter space corresponding to a mechanically-stable meniscus is significantly impacted by θ with hydrophilic wicks exhibiting the comparatively broader range of admissible ΔT and $T_{\rm op}$. This influence of surface wettability is due to the fact that any variation of the contact angle resets the position of the triple point leading to a modification in the breadth of the solution space. This modification is also seen in figure 6 (a), which shows the variation of the heat transfer, Q, with $T_{\rm op}$ and ΔT. Surfaces are drawn only where a mechanically-stable meniscus is anticipated; in turn, mechanically-stable menisci arise for a broader range of ΔT and $T_{\rm op}$ combinations when θ is small. Figure 6 (b) portrays similar effects but for different D/β; this

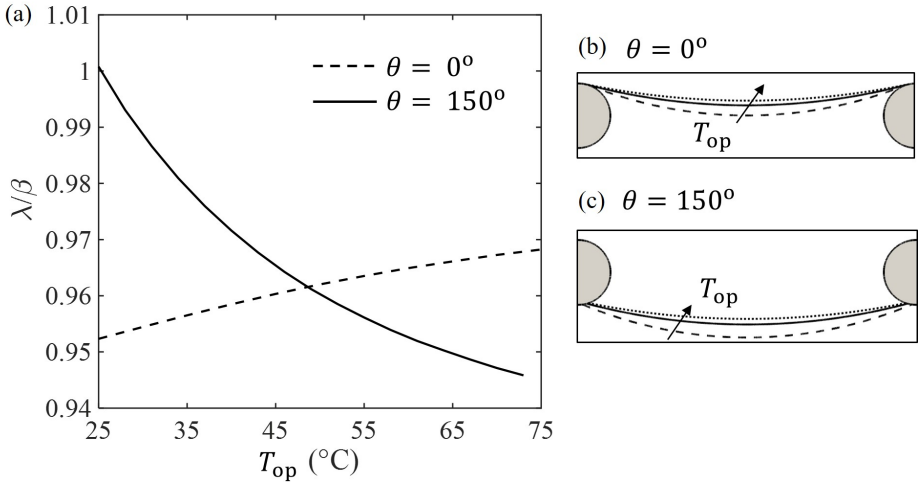


Figure 4: (a) Variation with $T_{\rm op}$ of the meniscus length for the same source-to-sink temperature difference ($\Delta T = 15^\circ$ C) but different contact angles. Illustration of the meniscus shape for $T_{\rm op} = 35^\circ$C, 45°C and 55°C for (b) $\theta = 0^\circ$ and (c) $\theta = 150^\circ$. Throughout, we assume $D/\beta = 0.35$.

figure will be discussed in section 3.3.

To further examine the narrowing of the parameter space that is evident most especially in figures 5 (d and h), a regime diagram has been constructed that shows the temperature combinations where a meniscus can form and remain mechanically-stable. Figure 7 (a) presents the solution space for a hydrophobic wick ($\theta = 150^\circ$) where the solid curve shows limiting combinations of $T_{\rm op}$ and ΔT for which (9) prescribes a physical solution. Even within this boundary of physically-acceptable solutions, however, there is the possibility that menisci from adjacent wire pairs may overlap in the neighborhood of a wire south pole. This region of overlap is indicated by the cross-hatched segment of the graph. Figure 7 (b) shows similar results but considers the impact of changing the contact angle. Note that the propensity to overlap adjacent menisci is significantly reduced as the wick is rendered more hydrophilic, e.g. even for $\theta = 120^\circ$, only a very narrow cross-hatched region is evident. For still smaller contact angles, and in the limit as $\theta \to 0^\circ$, we reproduce the results of Chi (1976). In contrast to the present study, Chi (1976) focuses on the largest possible capillary pressure, which is given from (8) as $P_{\rm c,max} = \sigma/R_{\rm min}$ where $R_{\rm min} = (\beta - D)/2$ resulting in a maximum capillary pressure of $2\sigma/(\beta - D)$. Chi (1976)'s focus on the case of maximum capillary pressure and minimum radius of curvature, though helpful in prescribing high-end performance limits, obscures the fact that the wicks of real heat pipes are not perfectly hydrophilic. In fact, and as we explore in further detail in section 4.1, wicks may be chemically-treated such that θ is made to vary with the axial coordinate.

3.3 Role of mesh number

Whereas figures 6 (a) and 7 (b) show that the breadth of the solution space is influenced by θ, we expect that the geometric parameters β and D should also exert some influence. This suspicion is confirmed by figures 6 (b) and 7 (c), where D/β is varied by changing the center-to-center distance between adjacent wires. Changing D/β (or, equivalently, the wick permeability) alters the wick thermal conductivity and hence, the heat flux, Q, as shown in figure 6 (b). As such, the pressures of the liquid and vapor phases to either side of the meniscus are likewise modified through (2) and (4). Figure 6 (b) confirms that a larger D/β is associated with higher heat loads but comes at the expense of a reduced parameter space where the menisci remain stable.

Consistent with figure 6 (b), the regime diagram in figure 7 (c) shows how the solution space is impacted by the variation of D/β. With increased β (such that $D/\beta = 0.25$ vs. 0.35 in figures 3,4,5,6 and 7 a,b), the solution spaces broaden as compared to those in figure 7 (b). Indeed, with increased wire-to-wire spacing, the wick permeability increases (by 2.72 times in this case). Hence, smaller pressure drops are predicted by (4) and these, in turn, are associated with smaller capillary pressures. Therefore, menisci remain mechanically-stable even at higher ΔT (or higher heat fluxes). Of course, there is a second way of achieving the value for D/β of 0.25 reported in figure 7 (c) and this is to decrease the wire diameter while keeping the spacing between the wires fixed. However, in this case, and relative to the base case of figure 7 (b), the wick permeability then increases by a factor of 1.37 rather than by 2.72. Correspondingly, curves different from those of figure 7 (c) featuring even narrower solution spaces will obtain.

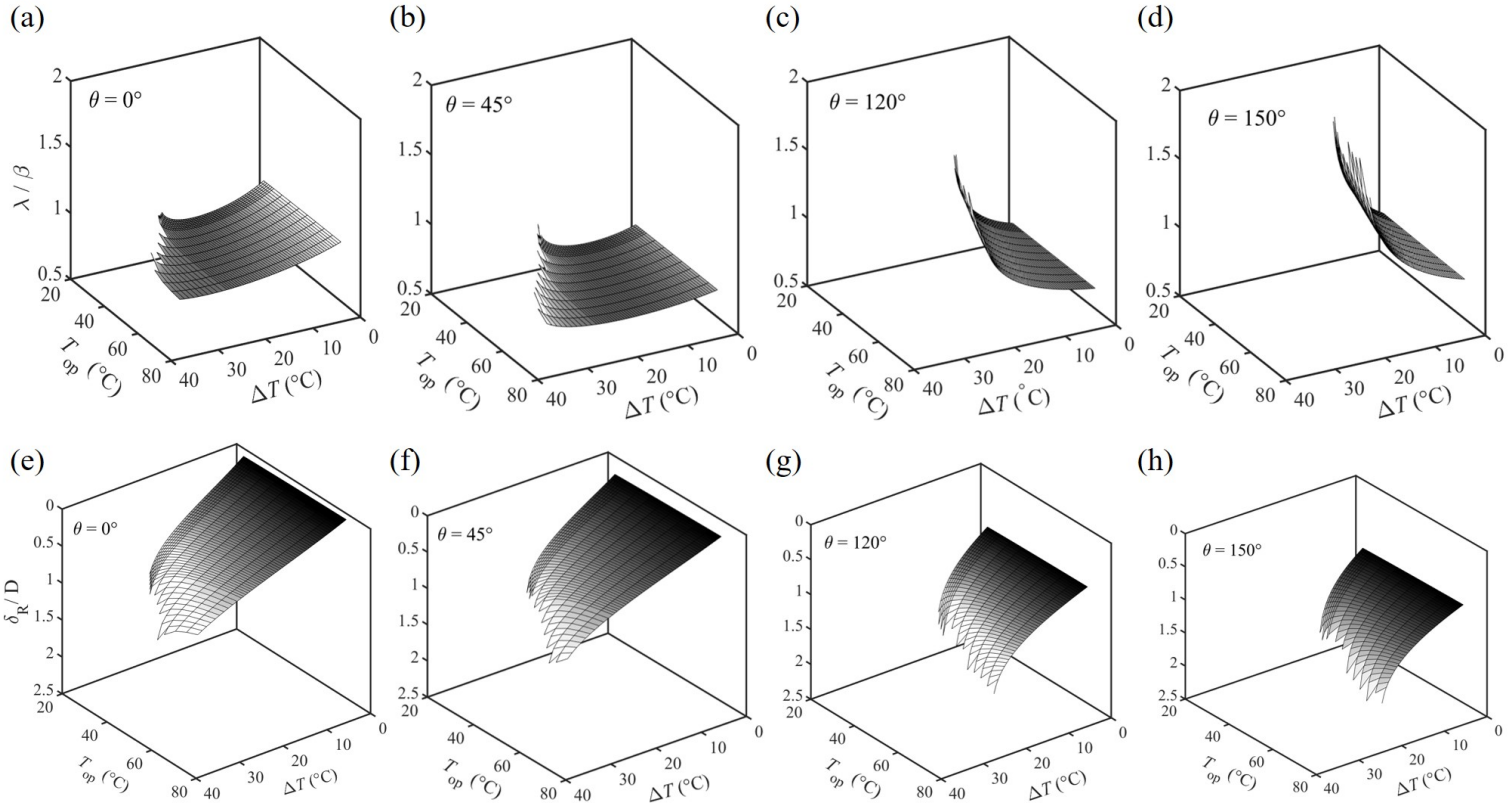


Figure 5: Variation of the meniscus length (a-d) and recess depth (e-h) with T_{op} and ΔT for (a,e) $\theta = 0°$ (b,f) 45° (c,g) 120° and (d,h) 150°. Throughout, we assume $D/\beta = 0.35$. Where no surface appears, no physically-acceptable solution to (9) is possible. In order to be consistent with the definition for δ_R provided schematically in figure 2, the vertical axis here is inverted.

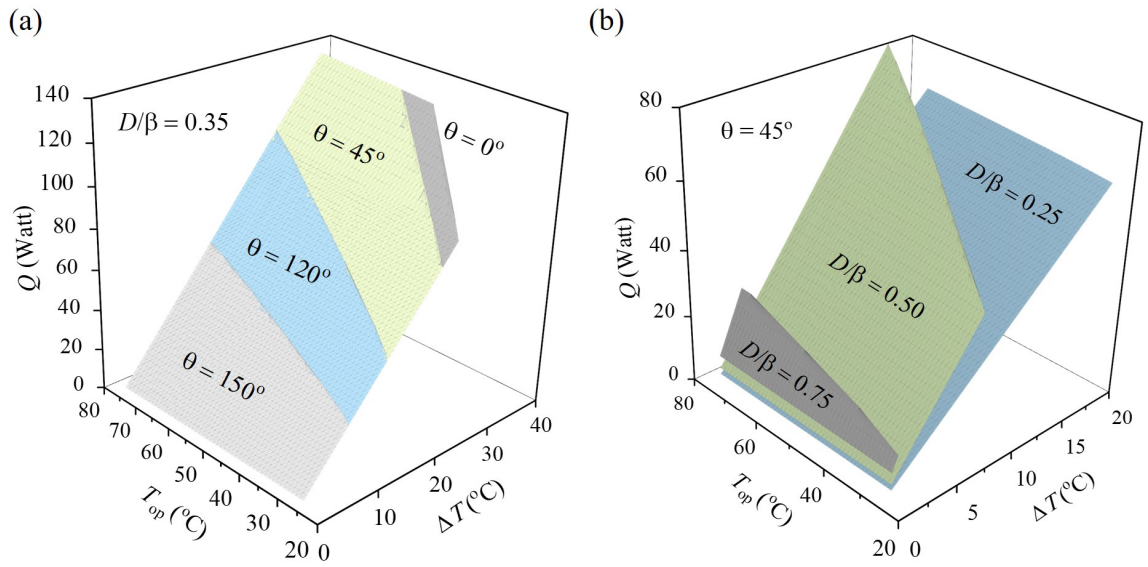


Figure 6: [Color online] Parameter space over which the meniscus forms and remains mechanically-stable (a) for different contact angles with fixed $D/\beta = 0.35$ and (b) for different D/β with fixed contact angle, $\theta = 45°$.

To further characterize the effect of the wire diameter and spacing on the details of the interface deflection, figure 8 shows the variation of the meniscus length and recess depth with $T_{\rm op}$ and ΔT for $\theta = 45°$ and three different choices of D/β. The wire-to-wire spacing impacts not only the meniscus length and the degree to which it is recessed but also, consistent with figures 6 (b) and 7 (b,c), the breadth of the parameter space where a mechanically-stable meniscus can form. In figures 8 (a,d), where β assumes the smallest value, menisci for different combinations of $T_{\rm op}$ and ΔT are short and arise over only a limited segment of the parameter space. As β increases (figures 8 b,e), the corresponding menisci are longer and exhibit a lesser degree of recession. For comparatively large β (i.e. figures 8 c,f where the wire spacing is four times larger than the wire diameter), menisci are, as expected, much longer. Figure 8 confirms that small menisci and large δ_R come at the cost of a more limited parameter space as compared to, say, figures 8 (c,f) ; as β increases, longer menisci arise and these are mechanically-stable over a larger range of ΔT.

Results from figure 8 are reproduced in figure 9 (a-c) with D/β replacing ΔT as one of the independent variables. These three panels of figure 9 consider three different contact angles and, consistent with figures 5, we find different parametric ranges corresponding to physically-acceptable solutions. Further insight into the admissible parametric range is provided by figure 9 (d,e) where we illustrate schematically how the contact angle sets the position of the triple point, modifies the meniscus length and also dictates whether or not meniscus overlap will occur. In figure 9 (d), λ decreases as the contact angle varies from 0° to 45° and the meniscus is pushed toward the equatorial plane. As θ is increased to 120°, the meniscus is pushed through this plane and λ increases as a result. This trend continues for further

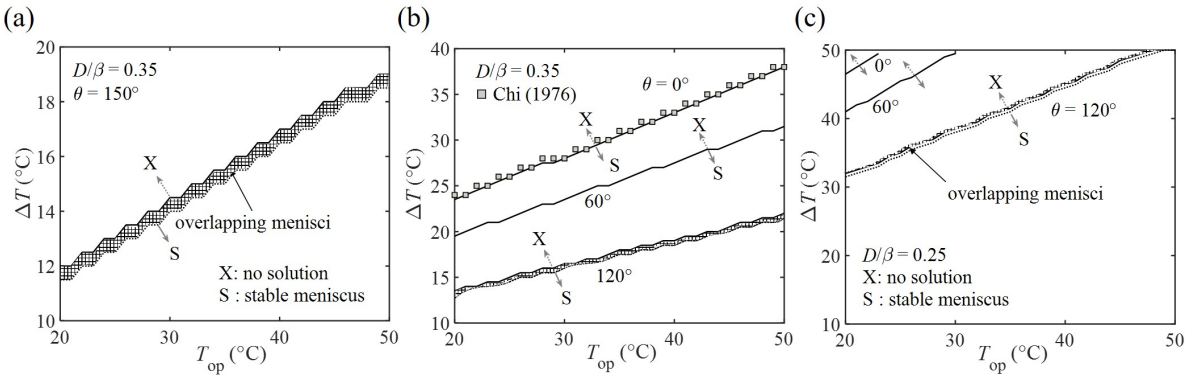


Figure 7: Regime diagrams showing the portion of (T_{op}, ΔT) space conducive to meniscus formation: (a) The solid curve shows the limiting values for T_{op} and ΔT below which a mechanically-stable interface is anticipated. The crosshatched region shows T_{op} and ΔT combinations where menisci are mechanically-stable but overlapping. Above the solid curve, menisci are mechanically-unstable. Here $\theta = 150°$ and $D/\beta = 0.35$ ($D = 6.25 \times 10^{-2}$ mm). Panel (b) is similar to panel (a) but shows the effect of changing θ. Panel (c) is similar to panel (b) but considers a larger spacing between adjacent wires such that $D/\beta = 0.25$. The jagged character of the lines in panel (a) is due to discretization limitations; these are progressively relaxed as the temperature range is broadened in panels (b) and (c). Analogously, note that the panels have different vertical axis limits.

increases of the contact angle until a point of meniscus overlap is reached, which for this particular configuration arises when $\theta = 169.5°$. The corresponding critical angle for the case $D/\beta = 0.5$ is smaller, *i.e.* $\theta = 72°$. As such, and in figure 9 (e), we show the meniscus shape for $\theta = 0°$ and $\theta = 45°$ but not for $\theta = 120°$. In conclusion, a smaller D/β broadens the parameter space as well as the range of contact angles over which physically-acceptable solutions may be realized. Such a small D/β is, however, associated not only with a depressed heat flux (figure 6 b) but also longer interface lengths and shallower recess depths, both of which are disadvantageous vis-à-vis liquid entrainment. The situation is therefore similar to the choice of θ as explored in figures 5 (e-h), 6 (a) and 7, *i.e.*, rendering the wick hydrophobic leads to larger δ_R but also constrains the solution to live in a smaller parameter space.

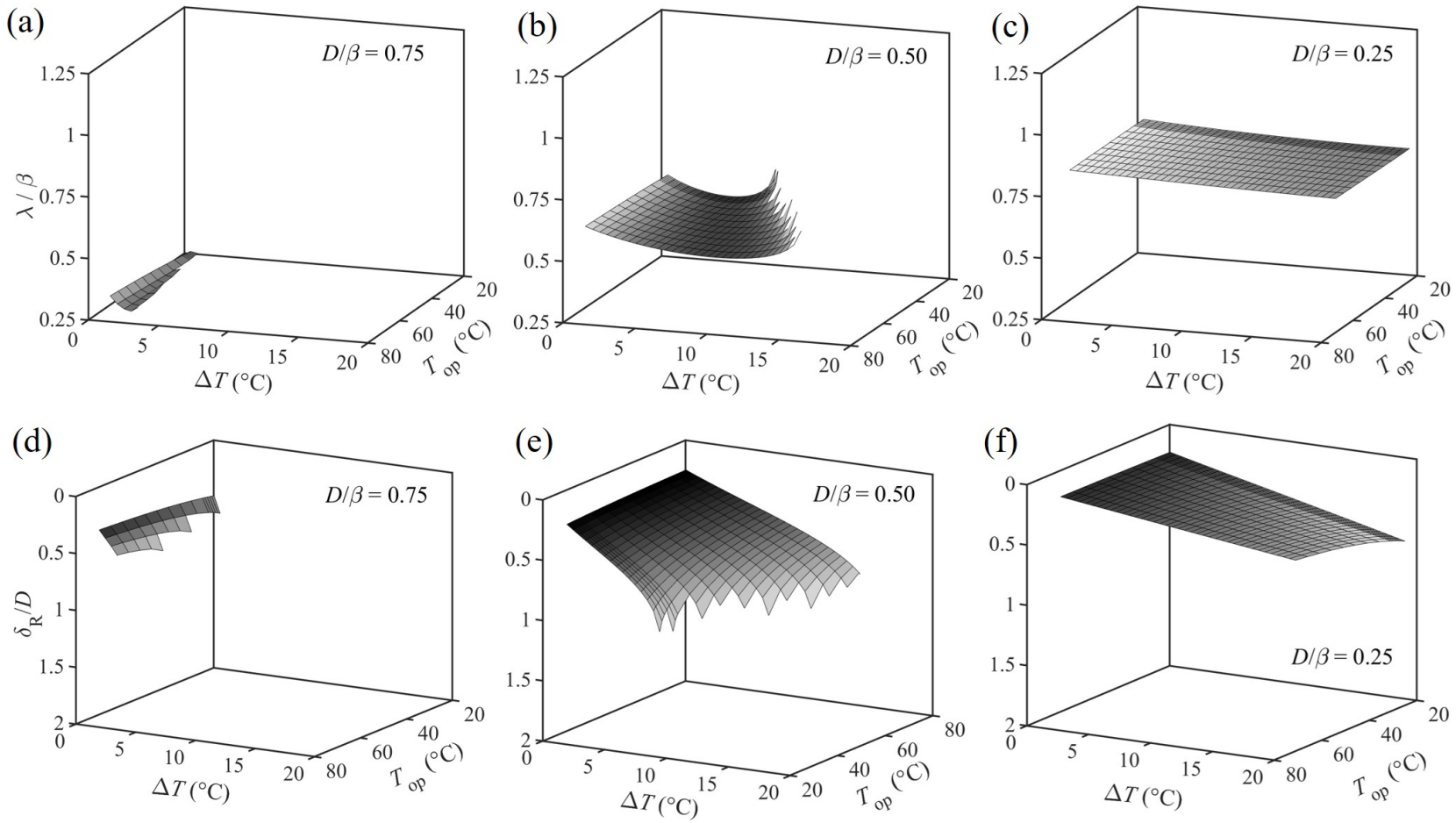


Figure 8: Effect of wire spacing on meniscus length (a-c) and recess depth (d-f): $D/\beta =$ (a,d) 0.75 (b,e) 0.5 and (c,f) 0.25. Throughout, we assume $\theta = 45°$.

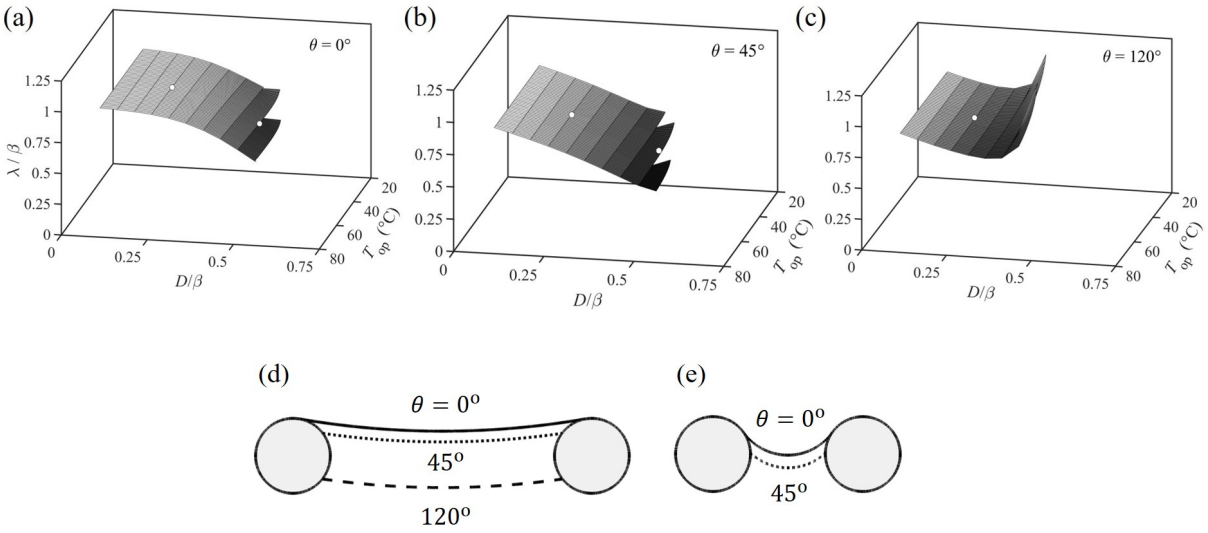


Figure 9: (a-c) Meniscus length as a function of D/β and the operating temperature for various contact angles. (a) $\theta = 0°$, (b) $\theta = 45°$ and (c) $\theta = 120°$. In all cases, $\Delta T = 10°$C. The left white dots in each of the panels denote $D/\beta = 0.25$ and $T_{\rm op} = 50°$C and the right white dots in panel (a) and (b) denote $D/\beta = 0.5$ and $T_{\rm op} = 50°$C. Menisci corresponding to the left and right white dots are illustrated, respectively, in panels (d) and (e).

4 Results – global analysis

Up until now, we have examined how the meniscus shape varies with different thermodynamic parameters, θ, $T_{\rm op}$, ΔT etc. Although this previous analysis has largely been restricted to an examination of a particular meniscus, any change to θ, $T_{\rm op}$ and/or ΔT will modify each of the menisci formed from the evaporator to the condenser end. Here, we characterize this overall effect.

Figure 10 illustrates how the recess depth and meniscus length change as a function of axial position. For a wick with a uniform contact angle of $\theta = 0°$, menisci near the evaporator end are recessed whereas those near the condenser end tend to flood the wick. Such kind of flooding is avoided for a hydrophobic wick with $\theta = 100°$; here, however, the evaporator is considerably de-wetted. For an intermediate uniform wettability of $\theta = 55°$, the minimum of the interface is very slightly recessed below the equatorial plane at the evaporator end, but not so at the condenser end. As regards the meniscus length or, equivalently, the meniscus area, figure 10 (c) confirms that hydrophilic wicks offer larger surface areas than do their more hydrophobic counterparts. Also included in figure 10 are two cases for which the wettability varies with axial position, i.e. $\theta = \theta(x)$; these will be discussed in section 4.1.

Now that the axial variation of individual meniscus lengths and recess depths have been examined, we proceed to characterize the liquid-vapor interface whose length (Λ) is deter-

mined through the following sum:

$$\Lambda = \sum_{i=1}^{\mathcal{N}_{\text{adia}}-1} \lambda_i$$

Figure 11 (a) shows the variation of Λ with θ for $T_{\text{op}} = 35°\text{C}$ and $\Delta T = 5°\text{C}$, 10°C and 15°C. Here, the interface length is non-dimensionalized by Λ_{min}, the minimum observed interface length, which is realized for the smallest axial temperature difference. For all three curves from figure 11 (a), the shortest interface length corresponds neither to a hydrophilic nor a hydrophobic wick, but rather to something in between where $\theta = \theta_{\text{cr}}$. Also, wicks that are strongly hydrophilic (hydrophobic) show a decrease (increase) in Λ with ΔT.

Related to Λ is the liquid volume entrapped within the wick. For the 2D system of interest here, we consider a volume per unit depth into the page, denoted as A and determined as

$$A = \sum_{i=1}^{\mathcal{N}_{\text{adia}}-1} a_i$$

where a_i is the volume of the entrapped liquid within individual cell and defined via

$$\frac{a_i}{2} = \begin{cases} \int_{-\beta/2}^{-s/2} \gamma \, \mathrm{d}x + \int_{-s/2}^{0} \eta \, \mathrm{d}x - a_x & \text{triple point above the equatorial plane} \\ \int_{-\beta/2}^{-s/2} \gamma \, \mathrm{d}x + \int_{-s/2}^{0} \eta \, \mathrm{d}x & \text{triple point below the equatorial plane} \\ \int_{-\beta/2}^{0} \eta \, \mathrm{d}x & \text{triple point at the south pole} \end{cases} \tag{12}$$

Here a_x is the volume occupied by the wires (Harris & Stöcker 1998), *i.e.*,

$$a_x = \frac{D^2}{4} \arccos\left(\frac{D-2H}{D}\right) - \left(\frac{D}{2} - H\right)\sqrt{DH - H^2}$$

where s and H are shown in figure 2, $\gamma = \gamma(x)$ is a function that defines the shape of the circular wire and $\eta = \eta(x)$ is defined in (1). The effect of wettability on the entrapped liquid volume is illustrated in figure 11 (b) where the liquid volume is non-dimensionalized by the volume of a just-flooded wick. Thus A_{flood}, which equivalently represents the maximum volumetric capacity of the wick, is determined by connecting the wire north poles with flat menisci corresponding to a contact angle of 0°. Consistent with figure 9, figure 11 (b) indicates that increasing θ will cause the interface to shift downwards leading to a drop (albeit modest for this choice of the offset distance, d_{off}) in the volume of entrapped liquid.

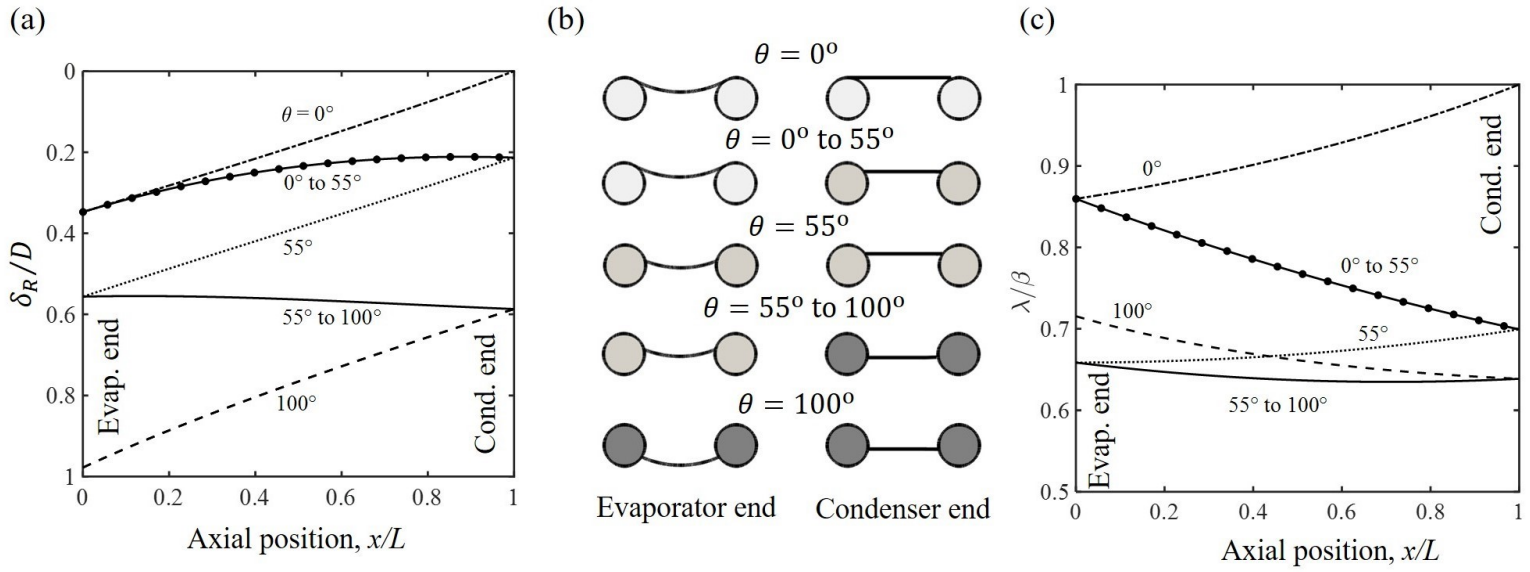


Figure 10: Axial variation of (a) the recess depth, and (c) interface length along the heat pipe adiabatic section. Dashed, dotted and dash-dotted lines show the variation for Scheme 1 where contact angles are set at 100°, 55° and 0°, respectively. Continuous lines are for Scheme 2 with θ varying from 55° to 100°, and from 0° to 55°. Panel (b) schematically illustrates the end-member meniscus shapes for each of the corresponding cases from panels (a) and (c).

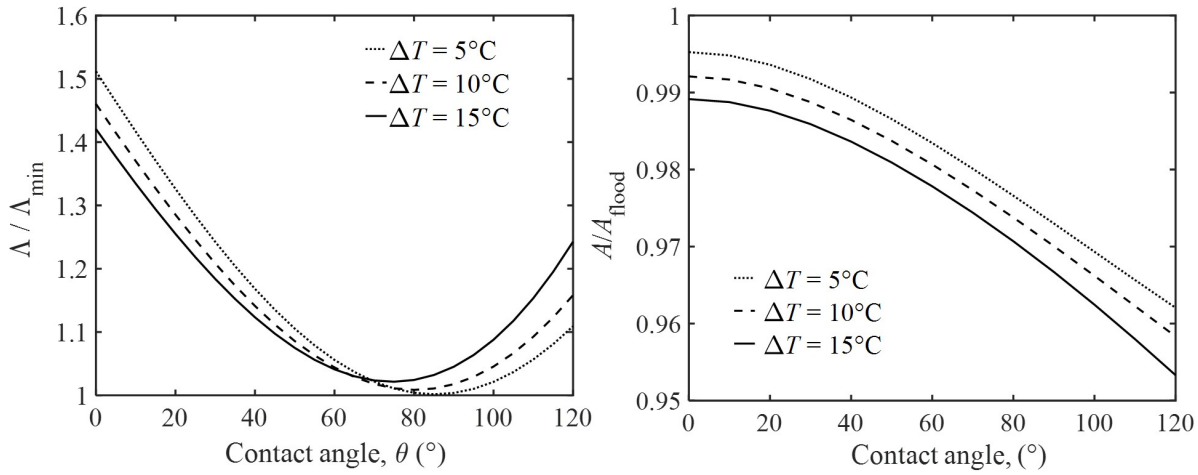


Figure 11: Variation of (a) interface length, Λ, and (b) entrapped liquid volume, A, with contact angle for $D/\beta = 0.35$ and $T_{\text{op}} = 35°\text{C}$.

4.1 Axial wettability gradient

One major challenge in designing heat pipes is to minimize entrainment without compromising the efficacy of heat transfer. Entrainment results from the counter-flow of vapor and liquid, which serves to perturb the interface through a Kelvin-Helmholtz instability (Nguyen-Chi & Groll 1981). This problem is more pronounced for larger heat load, whereby vapor velocities can be large. A possible remedy is to chemically-treat the wires so as to recess the interface below the equatorial plane of the wires that make up the wick (Williams & Harris 2005). Such a treatment serves a further purpose at the condenser end, i.e. by exposing more of the wires to vapor, drop-wise condensation is promoted (Rykaczewski et al. 2011, Enright et al. 2014), which has the advantage of efficient droplet nucleation and self-removal (Chen et al. 2011). On the other hand, an interface that is highly recessed at the evaporator end does not facilitate film-wise evaporation, and this may lead, in turn, to dry-out and a dramatic performance drop (Cheng & Mewes 2012). Hence it is important to maintain sufficient contact of liquid and solid close to the evaporator section even if efforts are undertaken to otherwise minimize entrainment. To this end, application of a surface exhibiting a wettability gradient wherein the evaporator and condenser ends are respectively rendered hydrophilic and hydrophobic is reported to have enhanced the heat transfer for grooved heat pipes (Singh et al. 2017, Hu et al. 2013). Although an exhaustive thermo-fluid analysis of this observation is beyond the scope of the present study, it provides a sensible starting point for understanding how a spatially-variable contact angle will impact the shape of the interface along the length of the heat pipe. Quantitative details are provided in figure 10, which considers two cases where θ is a linear function of the axial position, x. In one case, the terminal values of the contact angle are 0° (evaporator end) and 55° (condenser end); in another, they are 55° (evaporator end) and 100° (condenser end). For the latter case, the solid line in figure 10 (a) shows that a nearly constant value for δ_R is obtained. Greater axial variations of δ_R are

noted when $0^\circ \leq \theta \leq 55^\circ$ where, in any event, the interface is situated above the equatorial plane.

Of course, the degree of entrainment depends not only on the recess depth, but also on the interfacial area or, more simply, the meniscus length (Ishii & Grolmes 1975). To this end, figure 10 (c) indicates that the chemical treatment favoring larger contact angles is again preferred. Stated differently, between the two linearly varying wettability cases, when $0^\circ \leq \theta \leq 55^\circ$, the meniscus length is 20% longer at the evaporator end and 7% longer at the condenser end. By contrast, when $55^\circ \leq \theta \leq 100^\circ$, interface lengths are shorter than in any of the uniform θ cases including $\theta = 55^\circ$ and 100°. Therefore, and among the scenarios considered in figure 10, that with $55^\circ \leq \theta \leq 100^\circ$ may offer the best overall compromise between maximizing the recess depth, minimizing the interface length and facilitating film-wise evaporation vs. drop-wise condensation. Making a more precise statement requires that particular penalty functions be applied to entrainment and an undesirable mode of phase change. Such considerations are deferred to future studies.

5 Conclusion

This study presents a model to predict the evolution of the liquid-vapor interface in the adiabatic section of a heat pipe owing to variations of the thermo-fluid flow conditions. In formulating this model, the Darcy and Hagen-Poiseuille flow equations are combined with the Young-Laplace equation in conjunction with associated thermodynamical relations - this to relate the interfacial deflection with the bulk flow parameters. Thus, solving the system of equations (2-4,7-9) that relates the thermo-fluid conditions to the surface chemical characteristics, one can determine, as a function of the axial coordinate, the variation of the meniscus radius of curvature and the position of the triple point. In turn, these quantities allow for an evaluation of arc length, be this on a scale that is local (distance between two adjacent wires) or global (entire length of the adiabatic section). The parameter space over which a heat pipe can operate efficiently is dictated not only by the heat load and operating temperature but, perhaps more importantly, by the wick surface characteristics. A regime diagram has been constructed that illustrates how a hydrophobic wick surface and/or larger mesh number impose constraints on the range of the solution space. An examination of the overall liquid-vapor interface measured all the way along the adiabatic section shows that the interface length is a non-monotonic function of the wettability. As such, the minimum interfacial area corresponds neither to a hydrophilic nor a hydrophobic wick, but rather to an intermediate wettability.

A key contribution of this study concerns its insights into how wettability influences the efficacy of a heat pipe when a heterogeneous surface chemical treatment is applied. While the classical strategy (Wu & Peterson 1991, Khrustalev & Faghri 1994) of enhancing capillarity by rendering the wick more hydrophilic may result in a modest performance boost, such a strategy may fail at higher heat loads due to reduced condensation and a greater risk of entrainment. While a hydrophilic wick enhances film-wise evaporation by wetting the wick in the evaporator, there is the simultaneous possibility of flooding the condenser and thereby inhibiting the drop-wise condensation that is more conducive to high rates of phase change.

The above design dilemma can be resolved by encouraging film-wise evaporation by the application of a hydrophillic surface chemical treatment in the evaporator. By the same token, drop-wise condensation can be facilitated by the application of a hydrophobic surface chemical treatment in the condenser. We explore such a possibility in figure 11 where we investigate two profiles for θ, i.e. θ a linear function of x varying from 0° to 55° and from 55° to 100°. This analysis reveals that the latter alternative is helpful in minimizing the interface length whilst also maintaining a reasonably generous recess depth. By both measures, we therefore expect entrainment to be curtailed as compared, say, to a case where θ is uniform and less than 55°. While a direct experimental verification of these predictions is beyond the scope of this present study, the results are in accord with recent experimental (Hu et al. 2013) and numerical studies (Singh et al. 2017, 2018) that compare the efficacy of heterogeneous surface chemical treatment in enhancing heat pipe performance.

A key limitation of this study is the assumption of a perfect/ideal wick surface that respects the Young-Laplace equation and thereby gives a single equilibrium contact angle. However, in reality, surfaces are more likely to have micro-asperities such that contact angle hysteresis is expected (De Gennes et al. 2013). This is a topic that we intend to pursue in future studies. Also worthwhile would be to develop a numerical model to asses the effectiveness of interface recession to shield the liquid from the overlying and counterflowing vapor. Such an investigation could, for instance, parameterize the rate of entrainment with δ_R for various wick geometries and Weber numbers.

Acknowledgment: Funding for this study was generously provided by NSERC through a Collaborative Research and Development grant and by Airtex Manufacturing Partnership whose hospitality is further acknowledged.

Authorship contribution statement: MRF and PRW conceptualized the problem and secured the research fund. MRR and MRF developed the methodology, analysed the results and prepared the original draft. All authors reviewed and edited the draft.

Appendices

A Curvature radius and contact angle

The radius of curvature of the meniscus can be related to the contact angle using geometric identities. The schematic of figure 12 (a) shows two adjacent wires, which support a meniscus having a radius of curvature R. The meniscus makes a contact angle of θ with both wires, and the interface makes an angle ϕ with the horizontal. The angle $\angle CPQ$ measured through the triple point, P, equals 90^o. Consequently,

$$\angle CPK + \angle(90^o - \phi) + \angle(90^o - \theta) = 90^o \qquad \Rightarrow \angle CPK = \theta + \phi - 90^o$$

The horizontal distance between the triple point and the wire center, C, is $(D/2)\cos(\theta + \phi - 90^\circ) = (D/2)\sin(\phi + \theta)$. With this dimension to hand, we can now determine the half-horizontal separation distance between the wires, as measured along the plane of the triple point. This distance is

$$\frac{s}{2} = R\sin\phi = \frac{\beta}{2} - \frac{D}{2}\sin(\theta + \phi)$$

from which (9) follows directly.

From figure 12 (b), $\alpha + \theta + \phi = 180^\circ \Rightarrow \alpha = 180^\circ - (\theta + \phi)$. Note, however, that α is one-half of the angle of the intercepted arc described by the points PAP_o. In symbols, $\alpha = \frac{1}{2}\gamma$ where γ is defined in figure 12 (b). The angle γ is important when describing the vertical distance, $h_c = (D/2)\cos\alpha$, between the wire center and the triple point. Hence, the vertical distance between A and P is $h_t = (D/2)(1 - \cos\alpha)$. The above equation holds for cases when the meniscus touches the wire below the equatorial plane and hence $\alpha \leq 90^o$. When the triple point is instead located above the equatorial plane, $\alpha > 90^o$ and the expression for h_t reads $h_t = (D/2)(1 + \cos\alpha)$. Using these results and the offset distance, d_{off}, defined schematically in figure 1, we find that the ordinate of the triple point is

$$y_{m,t} = \begin{cases} d_{\text{off}} + (D/2)(1 - \cos\alpha) & \alpha \leq 90^o \\ d_{\text{off}} + (D/2)(1 + \cos\alpha) & \alpha > 90^o \end{cases}$$

Because α is a function of P_c, which varies with the axial coordinate, the shape of the menisci can now be determined as an a function of x. Accordingly, the variation of R with x can be ascertained. Once R is known, it is straightforward to compute λ from which we can construct figures such as figure 10 (c).

B Thermal resistance network model

The axial heat flux and temperatures internal to the heat pipe can be calculated by constructing an electrical circuit analogue as in figure 13. This schematic shows a simplified circuit

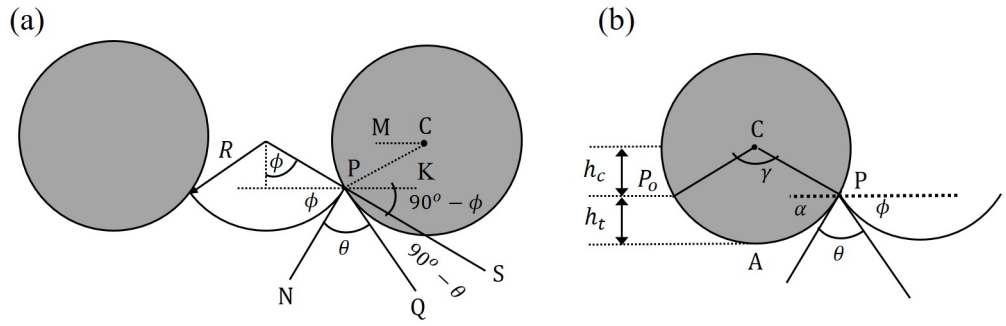


Figure 12: Meniscus geometry.

corresponding to a cylindrical heat pipe containing an interior wick. The radial resistances associated with the heat pipe wall (shell) and interior wick can be respectively evaluated as

$$R^r_{\text{shell}} = \frac{\log(d_o/d_i)}{2\pi L K_{\text{shell}}} \quad \text{and} \quad R^r_{\text{wick}} = \frac{\log(d_i/d_v)}{2\pi L K_{\text{eff}}} \tag{13}$$

where K_{shell} and K_{eff} respectively refer to the thermal conductivity of the heat pipe shell and of the saturated wick. Both of these thermal conductivities are functions of the operating temperature, T_{op}, which is determined from the arithmetic average of the end-point temperatures of the adiabatic section (Chi 1976, Abu-Eishah 2001, Ferrandi et al. 2013). Meanwhile, d_o, d_i, d_v denote, respectively, outer diameter, inner diameter and diameter of the vapor core. Resistance due to the liquid−vapor interface, R^r_{int}, is usually considered to be negligible (Peterson 1994).

The axial resistance, R^a_{vapor}, due to the vapor flow is usually very small, which indeed makes heat pipes efficient devices for transferring heat from the source to the sink. A commonly-accepted expression for R^a_{vapor} reads (Peterson 1994)

$$R^a_{\text{vapor}} = \frac{f_v \text{Re}_v}{2} \frac{\mu_v T_{\text{op}}}{\pi r_v^4 \rho_v^2 h_{fg}^2} (L_e/6 + L_a + L_c/6) \tag{14}$$

Here, $T_{\text{op}}, h_{\text{fg}}$ and ρ_v are, respectively, the operating temperature, the latent heat of vaporization and the vapor density while $f_v Re_v$ is the drag coefficient. The axial resistances of the shell, R^a_{shell}, and of the wick, R^a_{wick}, are several orders of magnitude larger than the resistances described above. As such, the thermal circuit can be considered open and non-thermally-conductive along the segments in question. This observation greatly simplifies the thermal network model, and an equivalent resistance can be defined as

$$R_{\text{eq}} = 2\left(R^r_{\text{wick}} + R^r_{\text{shell}}\right) + R^a_{\text{vapor}} \tag{15}$$

Consistent with the above remarks, the latter term from the right-hand side is typically much smaller than either of the radial thermal resistances. With increasing T_{op}, the thermal conductivities of the wick and of the container shell increase leading to a decrease in R^r_{wick}

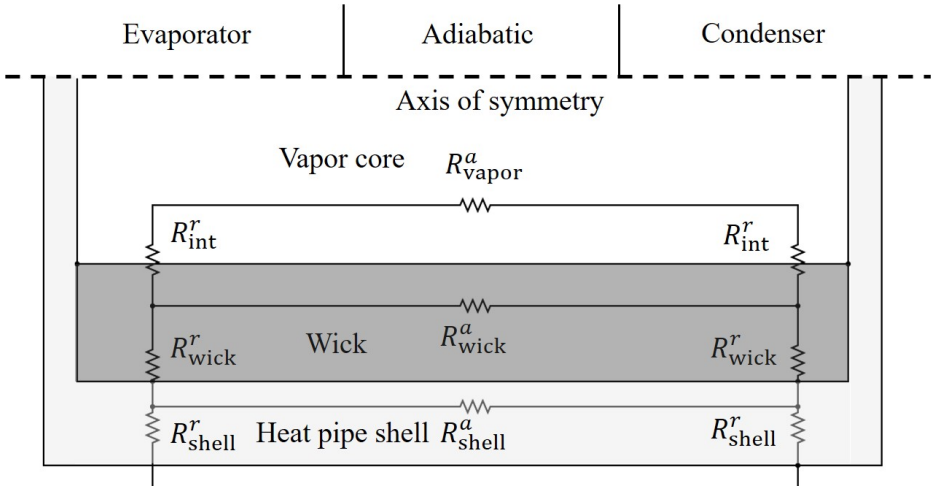


Figure 13: Thermal resistance network diagram (not to scale) showing the resistances at different sections of the heat pipe. R^a denotes an axial resistance and R^r denotes a radial resistance.

and R^r_{shell}. Further, and taking into consideration the variation of μ_v, ρ_v and h_{fg} with T_{op}, R^a_{vapor} also decreases as T_{op} increases. As such, R_{eq} decreases with increasing T_{op}.

For known values of the source and sink temperatures, the heat flux, Q, is readily determined from $Q = \frac{\Delta T}{R_{\text{eq}}}$, which is used to evaluate the mass flux, $\dot{m}$, in (2) and (4), without drawing any particular reference to the complicated processes of evaporation and condensation at the distal ends of the heat pipe (Chi 1976, Peterson 1994).

C Mechanical stability of the meniscus

We suppose that a meniscus whose shape is prescribed by (10 a) and exhibited schematically in figure 2 is perturbed such that it is displaced downward by some small distance. Such a perturbation could be associated with a flow of a small amount of liquid to a neighbouring cell. Adapting ideas from Princen (1969), there will result a decrease in the radius of curvature, which will, in turn, result in an increase of capillary pressure. The resulting suction will draw in liquid from the neighboring cells thereby restoring whatever liquid was lost when the interface was depressed. In this way, there is a natural restoring force that resists a destabilization of the interface as a whole.

When similar analyses are carried out for menisci described by (10 b) we find that a downward deflection of the meniscus leads to a decrease, not an increase, in the capillary pressure. This will initiate further liquid outflow from the perturbed cell, which will eventually collapse the meniscus. In this fashion, the meniscus prescribed by (10 b) is mechanically-unstable: any small perturbation will lead to an eventual breakdown of the vapor-liquid interface.

References

Abate, A. R., Thiele, J., Weinhart, M. & Weitz, D. A. (2010), 'Patterning microfluidic device wettability using flow confinement', *Lab on a Chip* **10**(14), 1774–1776.

Abu-Eishah, S. (2001), 'Correlations for the thermal conductivity of metals as a function of temperature', *International journal of thermophysics* **22**(6), 1855–1868.

Alduchov, O. A. & Eskridge, R. E. (1996), 'Improved magnus form approximation of saturation vapor pressure', *Journal of Applied Meteorology* **35**(4), 601–609.

Blossey, R. (2003), 'Self-cleaning surfaces—virtual realities', *Nature materials* **2**(5), 301–306.

Brahim, T. & Jemni, A. (2014), 'Effect of the heat pipe adiabatic region', *Journal of heat transfer* **136**(4).

Brown, O. L. (1951), 'The Clausius-Clapeyron equation', *Journal of Chemical Education* **28**(8), 428.

Bush, J. W. M., Hu, D. L. & Prakash, M. (2008), 'The integument of water-walking anthropods: Form and function', *Advances in Insect Physiology* **34**, 117–192.

Chen, X., Wu, J., Ma, R., Hua, M., Koratkar, N., Yao, S. & Wang, Z. (2011), 'Nanograssed micropyramidal architectures for continuous dropwise condensation', *Advanced functional materials* **21**(24), 4617–4623.

Cheng, L. & Mewes, D. (2012), *Advances in multiphase flow and heat transfer*, Vol. 3, Bentham Science Publishers.

Chi, S. (1976), *Heat pipe theory and practice*.

Daniel, S., Chaudhury, M. K. & Chen, J. C. (2001), 'Fast drop movements resulting from the phase change on a gradient surface', *Science* **291**(5504), 633–636.

De Gennes, P.-G., Brochard-Wyart, F. & Quéré, D. (2013), *Capillarity and wetting phenomena: drops, bubbles, pearls, waves*, Springer Science & Business Media.

Drelich, J., Chibowski, E., Meng, D. D. & Terpilowski, K. (2011), 'Hydrophilic and superhydrophilic surfaces and materials', *Soft Matter* **7**(21), 9804–9828.

Enright, R., Miljkovic, N., Alvarado, J. L., Kim, K. & Rose, J. W. (2014), 'Dropwise condensation on micro-and nanostructured surfaces', *Nanoscale and Microscale Thermophysical Engineering* **18**(3), 223–250.

Faghri, A. (2012), 'Review and advances in heat pipe science and technology', *Journal of heat transfer* **134**(12), 123001.

615 Feng, S., Wang, S., Gao, L., Li, G., Hou, Y. & Zheng, Y. (2014), 'Controlled directional
616 water-droplet spreading on a high-adhesion surface', *Angewandte Chemie International*
617 *Edition* **53**(24), 6163–6167.

618 Ferrandi, C., Iorizzo, F., Mameli, M., Zinna, S. & Marengo, M. (2013), 'Lumped parameter
619 model of sintered heat pipe: Transient numerical analysis and validation', *Applied thermal*
620 *engineering* **50**(1), 1280–1290.

621 Flynn, M. R. & Bush, J. W. (2008), 'Underwater breathing: the mechanics of plastron
622 respiration', *Journal of Fluid Mechanics* **608**, 275–296.

623 Fürstner, R., Barthlott, W., Neinhuis, C. & Walzel, P. (2005), 'Wetting and self-cleaning
624 properties of artificial superhydrophobic surfaces', *Langmuir* **21**(3), 956–961.

625 Gao, L., McCarthy, T. J. & Zhang, X. (2009), 'Wetting and superhydrophobicity', *Langmuir*
626 **25**(24), 14100–14104.

627 Harris, J. W. & Stöcker, H. (1998), *Handbook of mathematics and computational science*,
628 Springer Science & Business Media.

629 Hu, H., Wen, J., Bao, L., Jia, L., Song, D., Song, B., Pan, G., Scaraggi, M., Dini, D., Xue, Q.
630 et al. (2017), 'Significant and stable drag reduction with air rings confined by alternated
631 superhydrophobic and hydrophilic strips', *Science advances* **3**(9), e1603288.

632 Hu, Y., Cheng, J., Zhang, W., Shirakashi, R. & Wang, S. (2013), 'Thermal performance
633 enhancement of grooved heat pipes with inner surface treatment', *International Journal*
634 *of Heat and Mass Transfer* **67**, 416–419.

635 Ishii, M. & Grolmes, M. (1975), 'Inception criteria for droplet entrainment in two-phase
636 concurrent film flow', *AIChE Journal* **21**(2), 308–318.

637 Jenkins, H. D. B. (2008), *Chemical thermodynamics at a glance*, John Wiley & Sons.

638 Khrustalev, D. & Faghri, A. (1994), 'Thermal analysis of a micro heat pipe', *ASME Journal*
639 *of Heat Transfer* **116**, 189–198.

640 Kobayashi, T., Shimizu, K., Kaizuma, Y. & Konishi, S. (2011), 'Novel combination of hy-
641 drophilic/hydrophobic surface for large wettability difference and its application to liquid
642 manipulation', *Lab on a Chip* **11**(4), 639–644.

643 Lafuma, A. & Quéré, D. (2003), 'Superhydrophobic states', *Nature materials* **2**(7), 457–460.

644 Lee, S.-H., Lee, C.-S., Kim, B.-G. & Kim, Y.-K. (2002), 'Quantitatively controlled nanoliter
645 liquid manipulation using hydrophobic valving and control of surface wettability', *Journal*
646 *of Micromechanics and Microengineering* **13**(1), 89.

Lemp, M. A., Holly, F. J., Iwata, S. & Dohlman, C. H. (1970), 'The precorneal tear film: I. factors in spreading and maintaining a continuous tear film over the corneal surface', *Archives of ophthalmology* **83**(1), 89–94.

McHale, G., Flynn, M. R. & Newton, M. I. (2011), 'Plastron induced drag reduction and increased slip on a superhydrophobic sphere', *Soft Matter* **7**(21), 10100–10107.

Mingjie et al. (2010), 'Bioinspired super-antiwetting interfaces with special liquid- solid adhesion', *Accounts of chemical research* **43**(3), 368–377.

Mwaba, M. G., Huang, X. & Gu, J. (2006), 'Influence of wick characteristics on heat pipe performance', *International journal of energy research* **30**(7), 489–499.

Nguyen-Chi, H. & Groll, M. (1981), 'Entrainment or flooding limit in a closed two-phase thermosyphon', *Journal of Heat Recovery Systems* **1**(4), 275–286.

Peterson, G. P. (1994), *An introduction to heat pipes: modeling, testing, and applications*, Wiley.

Polet, D. T., Flynn, M. R. & Sperling, F. A. (2015), 'A mathematical model to capture complex microstructure orientation on insect wings', *PloS one* **10**(10).

Princen, H. (1969), 'Capillary phenomena in assemblies of parallel cylinders: I. capillary rise between two cylinders', *Journal of Colloid and Interface Science* **30**(1), 69–75.

Quéré, D. & Reyssat, M. (2008), 'Non-adhesive lotus and other hydrophobic materials', *Philosophical Transactions of the Royal Society A: Mathematical, Physical and Engineering Sciences* **366**(1870), 1539–1556.

Rastegari, A. & Akhavan, R. (2015), 'On the mechanism of turbulent drag reduction with super-hydrophobic surfaces', *Journal of Fluid Mechanics* **773**.

Reay, D., McGlen, R. & Kew, P. (2013), *Heat pipes: theory, design and applications*, Butterworth-Heinemann.

Richter, R. & Gottschlich, J. (1994), 'Thermodynamic aspects of heat pipe operation', *Journal of Thermophysics and Heat Transfer* **8**(2), 334–340.

Rykaczewski, K., Paxson, A. T., Staymates, M., Walker, M. L., Sun, X., Anand, S., Srinivasan, S., McKinley, G. H., Chinn, J., Scott, J. H. J. et al. (2014), 'Dropwise condensation of low surface tension fluids on omniphobic surfaces', *Scientific reports* **4**, 4158.

Rykaczewski, K., Scott, J. H. J., Rajauria, S., Chinn, J., Chinn, A. M. & Jones, W. (2011), 'Three dimensional aspects of droplet coalescence during dropwise condensation on superhydrophobic surfaces', *Soft Matter* **7**(19), 8749–8752.

679 Shafahi, M., Bianco, V., Vafai, K. & Manca, O. (2010), 'Thermal performance of flat-shaped
680 heat pipes using nanofluids', *International journal of heat and mass transfer* **53**(7-8), 1438–
681 1445.

682 Singh, M., Datla, N. V., Kondaraju, S. & Bahga, S. S. (2018), 'Enhanced thermal perfor-
683 mance of micro heat pipes through optimization of wettability gradient', *Applied Thermal*
684 *Engineering* **143**, 350–357.

685 Singh, M., Kondaraju, S. & Bahga, S. S. (2017), 'Enhancement of thermal performance
686 of micro heat pipes using wettability gradients', *International Journal of Heat and Mass*
687 *Transfer* **104**, 400–408.

688 Vafai, K. & Wang, W. (1992), 'Analysis of flow and heat transfer characteristics of an asym-
689 metrical flat plate heat pipe', *International journal of heat and mass transfer* **35**(9), 2087–
690 2099.

691 Williams, R. R. & Harris, D. K. (2005), 'The heat transfer limit of step-graded metal felt
692 heat pipe wicks', *International Journal of Heat and mass transfer* **48**(2), 293–305.

693 Wu, D. & Peterson, G. (1991), 'Investigation of the transient characteristics of a micro heat
694 pipe', *Journal of thermophysics and heat transfer* **5**(2), 129–134.

695 Zuo, Z. & Faghri, A. (1998), 'A network thermodynamic analysis of the heat pipe', *Interna-*
696 *tional Journal of Heat and Mass Transfer* **41**(11), 1473–1484.

Conflict of Interest

The authors declare no conflict of interest.